WILEY-VCH

Supporting Information

Nonlinear Terahertz Generation: Chiral and Achiral Meta-atom Coupling

Qingwei Wang, Xueqian Zhang, Quan Xu, Xi Feng, Yongchang Lu, Li Niu, Xieyu Chen, Eric Plum, Jianqiang Gu, Quanlong Yang, Ming Fang, Zhixiang Huang, Shuang Zhang, Jiaguang Han*, Weili Zhang**

Q. Wang, X. Zhang, Q. Xu, X. Feng, Y. Lu, L. Niu, X. Chen, J. Gu, J. Han
Center for Terahertz Waves and College of Precision Instrument and Optoelectronics Engineering, and the Key Laboratory of Optoelectronics Information and Technology, Tianjin University
Tianjin 300072, People's Republic of China
E-mail: alearn1988@tju.edu.cn, jiaghan@tju.edu.cn

E.Plum
Optoelectronics Research Centre and Centre for Photonic Metamaterials, University of Southampton
Highfield, Southampton SO17 1BJ, UK

Q. Yang
School of Physics and Electronics, Central South University
Changsha 410083, Hunan, People's Republic of China

M. Fang, Z. Huang
Key Laboratory of Intelligent Computing and Signal Processing, Ministry of Education, Anhui University
Hefei 230039, People's Republic of China

S. Zhang
Department of Physics, Faculty of Science, University of Hong Kong
Hong Kong 999077, People's Republic of China

W. Zhang
School of Electrical and Computer Engineering, Oklahoma State University
Stillwater, Oklahoma 74078, USA
E-mail: weili.zhang@okstate.edu

Formatted: German (Germany)

Supplementary Section S1. Coupled-mode theory analysis

The coupled system of the achiral meta-molecule under *y*-polarized illumination can be described well using coupled-mode theory:[S1]

$$\begin{cases} \frac{1}{2\pi}\frac{\partial}{\partial t}\begin{pmatrix}\psi_b\\ \psi_d\end{pmatrix} = i\begin{pmatrix} f_b & \kappa \\ \kappa & f_d\end{pmatrix}\begin{pmatrix}\psi_b\\ \psi_d\end{pmatrix} + \begin{pmatrix} -\gamma_b - \gamma_b' & \chi \\ \chi & -\gamma_d - \gamma_d'\end{pmatrix}\begin{pmatrix}\psi_b\\ \psi_d\end{pmatrix} + \begin{pmatrix} d_{1b} & d_{2b} \\ d_{1d} & d_{2d}\end{pmatrix}\begin{pmatrix}S_1^+\\ S_2^+\end{pmatrix} \\ \begin{pmatrix}S_1^-\\ S_2^-\end{pmatrix} = \begin{pmatrix} S_{11} & S_{12} \\ S_{21} & S_{22}\end{pmatrix}\begin{pmatrix}S_1^+\\ S_2^+\end{pmatrix} + \begin{pmatrix} d_{1b} & d_{1d} \\ d_{2b} & d_{2d}\end{pmatrix}\begin{pmatrix}\psi_b\\ \psi_d\end{pmatrix} \end{cases}, \quad \text{(S1)}$$

where $\Psi_{b,d}$, $f_{b,d}$, $\gamma_{b,d}$, and $\gamma'_{b,d}$ are the complex resonance amplitude, resonance frequency, radiation loss rate, and absorption loss rate with the subscript *b* and *d* representing the bright mode (electric dipole resonance) and the dark mode (magnetic dipole resonance), κ and χ are the near-field and far-field coupling strength between the bright mode and the dark mode, S_1^+ and S_2^+ are the inputs from the substrate side (port 1) and the structure side (port 2) whereas S_1^- and S_2^- are the outputs from port 1 and port 2, d_{im} is the excitation strength between the input and the resonance mode with $i = 1, 2$ and $m = b, d$, and S_{ij} is the background *S*-parameter between the inputs and outputs in the absence of bar resonator and SRRs with $j = 1, 2$.

Here, the system is excited merely from the substrate side, hence $S_2^+ = 0$. As the dark mode is non-radiative to the far field because of a π phase difference in the two SRRs, $\gamma_d = d_{1d} = d_{2d} = 0$. Meanwhile, the polarization of the dark mode is orthogonal to that from the bright mode, resulting in $\chi = 0$. According to the time-inversion symmetry and the energy conservation law, we have $|d_{1b}|^2 + |d_{2b}|^2 = 2\gamma_b$ and $d_{2b} = \eta d_{1b}$, where $\eta = n^{1/2}$ describes the asymmetry of the modes' radiations toward the two ports due to the presence of the quartz substrate ($n = 1.44$). For the applied quartz substrate, $S_{11} = (n - 1)/(1 + n)$, $S_{12} = S_{21} = 2n^{1/2}/(1 + n)$, and $S_{22} = (1 - n)/(1 + n)$. By submitting them to Equation S1, the reflection and transmission coefficients can be calculated as:

$$r = \frac{S_1^-}{S_1^+} = S_{11} + \frac{d_{1b}^2 \times \left[i(f - f_d) + \gamma_d' \right]}{\left[i(f - f_b) + \gamma_b + \gamma_b' \right] \times \left[i(f - f_d) + \gamma_d' \right] + \kappa^2}, \quad \text{(S2)}$$

$$t = \frac{S_2^-}{S_1^+} = S_{21} + \frac{\eta \times d_{1b}^2 \times \left[i(f - f_d) + \gamma_d' \right]}{\left[i(f - f_b) + \gamma_b + \gamma_b' \right] \times \left[i(f - f_d) + \gamma_d' \right] + \kappa^2}, \quad \text{(S3)}$$

respectively. Here, f is the frequency. Figure S4a shows the measured transmittance spectra and the corresponding fitted spectra $|t|^2$ of the four samples with different ΔS under y-polarized illumination. The fitted model matches the experimental results closely in all cases. The fitting parameters with increasing ΔS are plotted in Figure S4b-d. It is observed that the near field coupling strength κ monotonically increase with ΔS.

To get further insight into the near-field interaction between the bar resonator and SRRs, the complex resonance amplitudes Ψ_b and Ψ_d are derived from Equation S1:

$$\psi_b = \frac{d_{1b} \times \left[i(f - f_d) + \gamma_d' \right]}{\left[i(f - f_b) + \gamma_b + \gamma_b' \right] \times \left[i(f - f_d) + \gamma_d' \right] + \kappa^2} S_1^+, \quad \text{(S4)}$$

$$\psi_d = \frac{i \times \kappa \times d_{1b}}{\left[i(f - f_b) + \gamma_b + \gamma_b' \right] \times \left[i(f - f_d) + \gamma_d' \right] + \kappa^2} S_1^+. \quad \text{(S5)}$$

It is worth noting that, in the vicinity of resonance frequency f_d, the bright and dark modes will obtain a phase difference of π/2, while the resonance strength of the dark mode can be modulated by controlling κ. This phase difference and control over the dark mode's strength enable the handedness-selective response that we demonstrate for chiral meta-molecules.

Supplementary Section S2. Linear simulation

The commercial software COMSOL Multiphysics is used to design and simulate the linear electromagnetic properties of the proposed meta-molecules. All simulations are carried out by placing the relevant meta-molecule on a fused quartz substrate with periodic boundary conditions along the x and y directions. Gold is described by the Drude model $\varepsilon(\omega) = \varepsilon'(\omega) - i\varepsilon''(\omega) = \varepsilon_\infty - \omega_p{}^2/(\omega^2 + i\omega\gamma)$, where ε_∞ is the infinite frequency permittivity, ω_p is the plasma frequency and γ is the collision frequency. These parameters are set as $\varepsilon_\infty = 1$, $\omega_p = 1.4 \times 10^{16}$ rad·s^{-1} and $\gamma = 3.1 \times 10^{14}$ rad·s^{-1}. To check the strength of the magnetic dipole resonance, a probe is placed at the center of the SRR to record the H_z magnetic field component. According to the nonlinear polarization equation $P_{\mathrm{THz}} = \varepsilon_0 \chi^{(2)}_{\mathrm{THz}} E_1 E_2^*$ with ε_0 being the vacuum permittivity, $\chi^{(2)}_{\mathrm{THz}}$ being the effective 2nd-order nonlinear susceptibility, and E_1 and E_2 being the pump fields whose frequency difference locates at THz frequencies. As the THz frequencies are much smaller than the pump frequencies, the amplitude of the generated THz wave is approximately proportional to $|E|^2$ and thus $|H_z|^2$.

Formatted: English (United Kingdom)

Field Code Changed

Field Code Changed

Supplementary Section S3. Nonlinear simulation

The nonlinear process which originated from the incoming electromagnetic fields with the free electrons in the plasmonic structures is governed by[S2]

$$\nabla \times \mathbf{H} = \varepsilon_0 \frac{\partial \mathbf{E}}{\partial t} + \frac{\partial \mathbf{P}}{\partial t}, \tag{S6}$$

$$\nabla \times \mathbf{E} = -\mu_0 \frac{\partial \mathbf{H}}{\partial t}, \tag{S7}$$

$$\frac{\partial \boldsymbol{v}}{\partial t} + (\boldsymbol{v} \cdot \nabla)\boldsymbol{v} = -\frac{e}{m_e}(\mathbf{E} + \mu_0 \boldsymbol{v} \times \mathbf{H}) - \gamma \boldsymbol{v} - \frac{\nabla p}{n}, \tag{S8}$$

$$\frac{\partial n}{\partial t} = -\nabla \cdot (n\boldsymbol{v}), \tag{S9}$$

where $\boldsymbol{E}$, $\boldsymbol{H}$ and $\mathbf{P}$ are the electric field, magnetic fields and polarization vector; e, m_e, γ, n, and $\mathbf{v}$ are the electron charge, mass, collision frequency, density, and velocity, respectively; $p = (3\pi)^{2/3}(\hbar/5)n^{5/3}$ represents the quantum pressure.

To efficiently solve the above equations, finite-difference time-domain (FDTD) algorithm is implemented. Figure S6a illustrates a unit cell in the nonlinear simulation. The pump infrared laser pulse is illuminated onto the unit cell from the z direction and introduced using total-field and scattered-field (TF/SF) technique. It is described by a Gaussian pulse: $\boldsymbol{E}(t) = \boldsymbol{E}_0 \exp[-(2\ln 2)(t - t_0)^2/\tau^2]\cos(2\pi ct/\lambda_0)$ where the pulse width and the peak amplitude are set as $\tau = 65$ fs and $E_0 = 7 \times 10^7$ V m^{-1} whereas the wavelength is tuned from 1160 nm to 1500 nm according to the experiments. Uniform spatial steps $\Delta x = \Delta y = \Delta z = 2.5$ nm and time step $\Delta t = 3 \times 10^{-18}$ s are adopted. The nonlinear simulation results corresponding to the measured results are illustrated in Figure S6b-d.

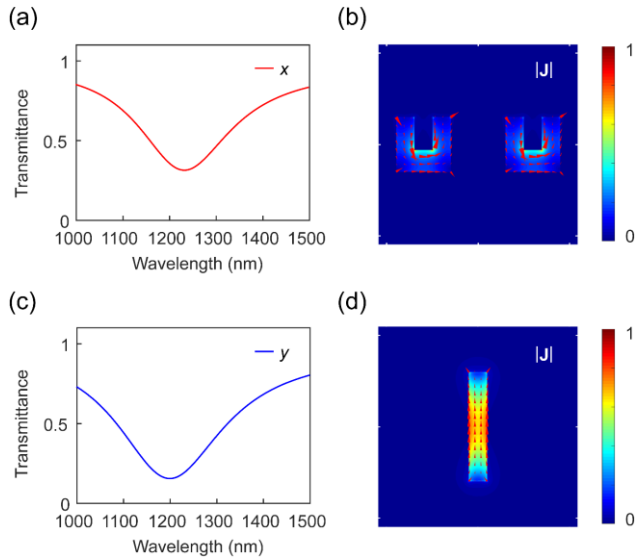

Figure S1. Simulated linear transmission spectra and surface current density distributions of the SRRs and the bar resonator. a,c) Simulated linear transmission spectra of the SRRs and the bar resonator under *x*- and *y*-polarized illuminations, respectively. b,d) Simulated surface current density distributions of the SRRs and the bar resonator under *x*- and *y*-polarized illuminations at 1230 nm and at 1200 nm, respectively.

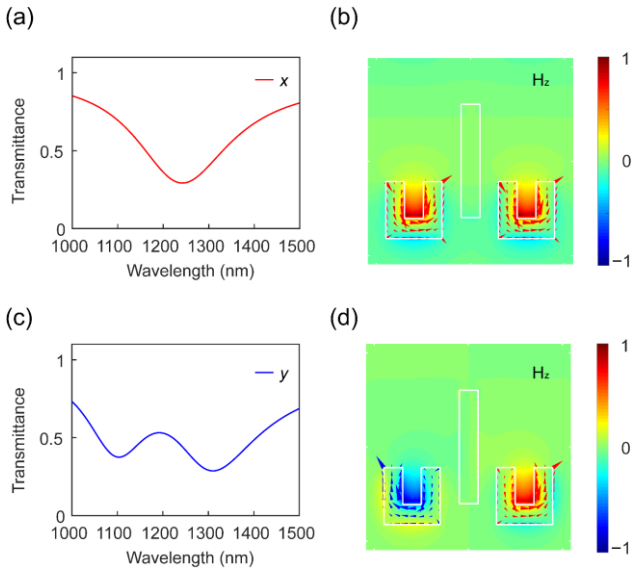

Figure S2. Simulated linear transmission spectra, H_z-field distributions and surface current distributions of achiral meta-molecule with ΔS = 130 nm. a,c) Simulated linear transmission spectra under *x*- and *y*-polarized illuminations, respectively. b,d) Simulated H_z-field and surface current distributions under *x*- and *y*-polarized illuminations at 1240 nm and at 1200 nm, respectively.

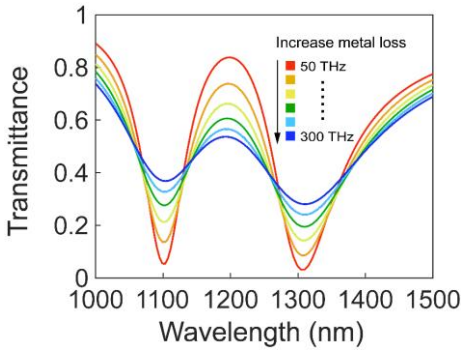

Figure S3. Simulated linear transmission spectra of the achiral meta-molecue at Δ*S* = 130 nm under *y*-polarized pump with increasing Ohmic loss in metal. These are obtained by increasing the collision frequency in the Drude model from 50 THz to 300 THz in a step of 50 THz. The results show that larger Ohmic loss corresponds to larger resonance absorption and thus weaker EIT window.

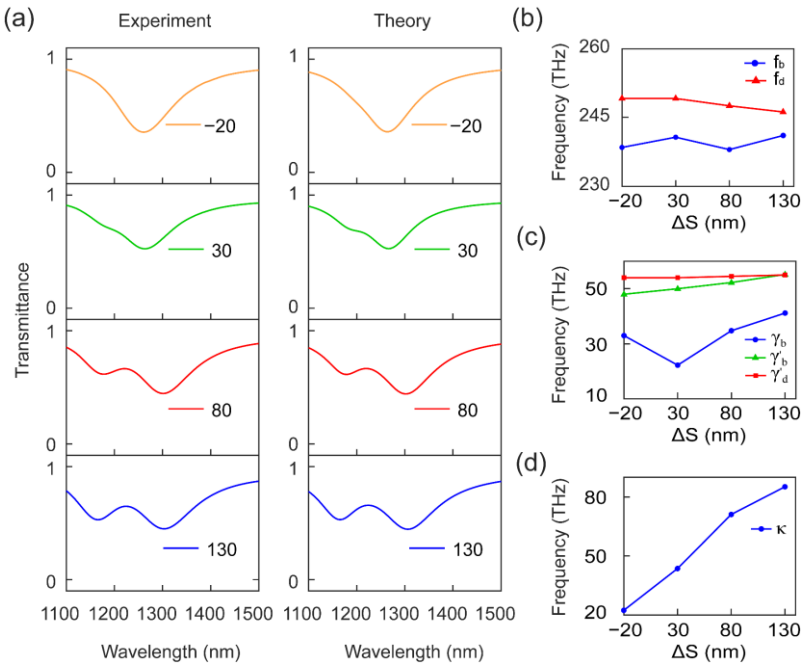

Figure S4. Coupled-mode theory fitting results for achiral meta-molecules. a) Measured and fitted transmission spectra for Δ*S* from −20 nm to 130 nm and incident *y*-polarization. b-d) Fitted resonance frequency $f_{b,d}$, radiation loss rate γ_b, absorption loss rate $\gamma'_{b,d}$, and near-field coupling strength κ with respect to Δ*S*.

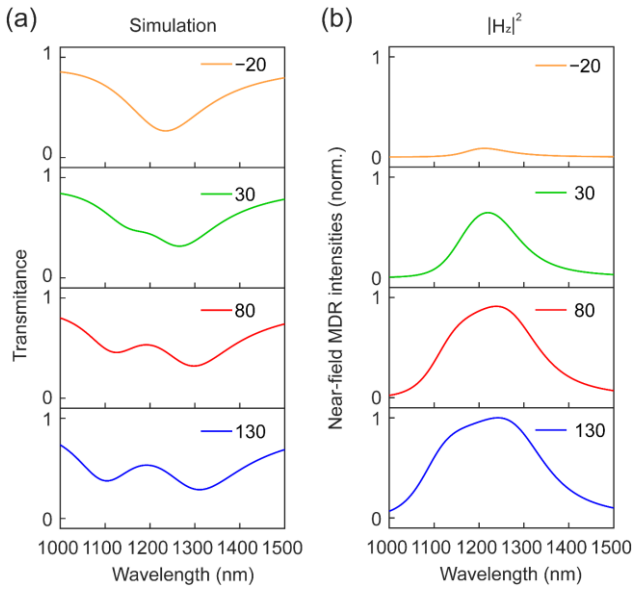

Figure S5. Simulated linear electromagnetic properties of achiral meta-molecules. a) Transmission spectra as ΔS changes from −20 nm to 130 nm under *y*-polarized illumination. b) Corresponding near-field MDR intensity spectra recorded as $|H_z|^2$ at the center of the SRRs.

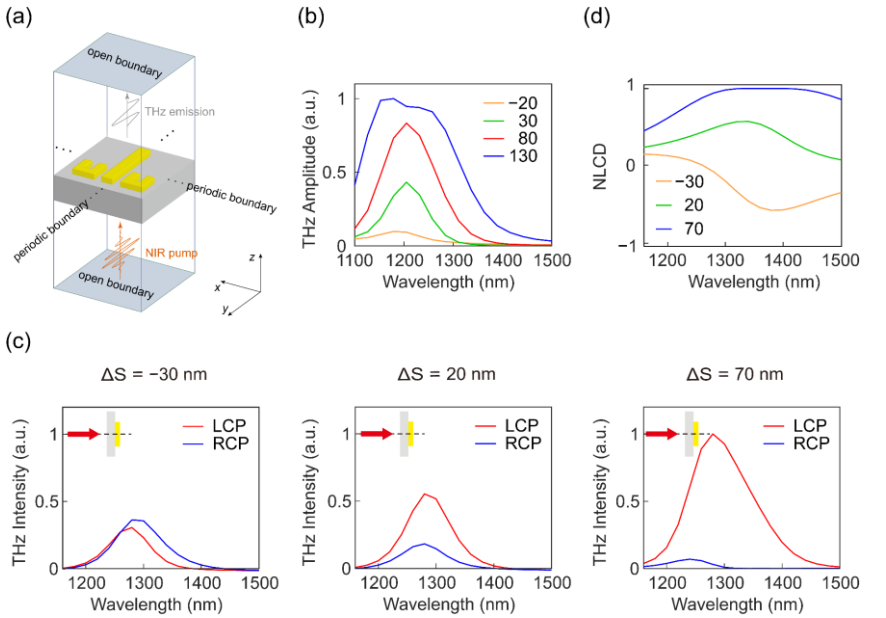

Figure S6. Nonlinear numerical simulations. a) Schematic of the nonlinear FDTD simulation setup. b) Simulated THz peak-to-peak amplitude as a function of the pump FW wavelength for achiral meta-molecules with ΔS changing from −20 nm to 130 nm under *y*-polarized illumination. c) Simulated THz intensity as a function of wavelength and handedness of the FW pump that illuminates the back side of the chiral meta-molecules. d) NLCD spectra calculated from the results in (c).

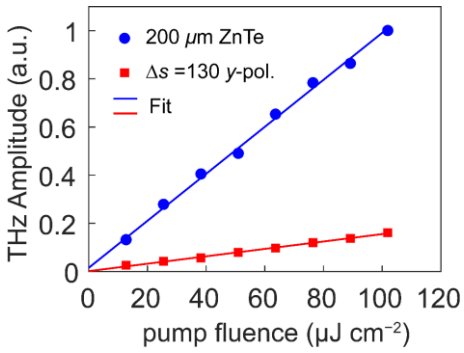

Figure S7. Measured THz peak-to-peak amplitudes as a function of the pump fluence. The results are measured from the achiral meta-molecule with ΔS = 130 nm under 1280 nm FW pump of *y*-polarized illumination and a 200 μm-thick ZnTe crystal under 800 nm FW pump. The peak-to-peak amplitude of the THz pulse generated from the ZnTe crystal is approximate 6.25 times of that from the nonlinear metasurface. In References S3, the measured conversion efficiency for a 500 μm-thick ZnTe under 800 nm FW pump is 3×10^{-5} at a 1.4 mJ cm^{-2} pump fluence. Taking the measured results at 101.9 μJ cm^{-2} pump fluence as an example, the conversion efficiency here is estimated to be $3 \times 10^{-5}/(13.7 \times 6.25^2 \times 2.5^2) = 0.9 \times 10^{-8}$, where the factor of 13.7 is the difference in pump fluence, 6.25 is the difference in the measured THz peak-to-peak amplitudes of the 200 μm ZnTe and the nonlinear metasurface, and 2.5 is the difference in crystal thickness. Though the conversion efficiency is low, the thickness of the nonlinear metasurface (48 nm) is about 10000 times thinner than the 500 μm-thick ZnTe crystal. Taking this factor into account, the effective conversion efficiency is about 40 times of the ZnTe crystal with the same thickness at 101.9 μJ cm^{-2} pump fluence.

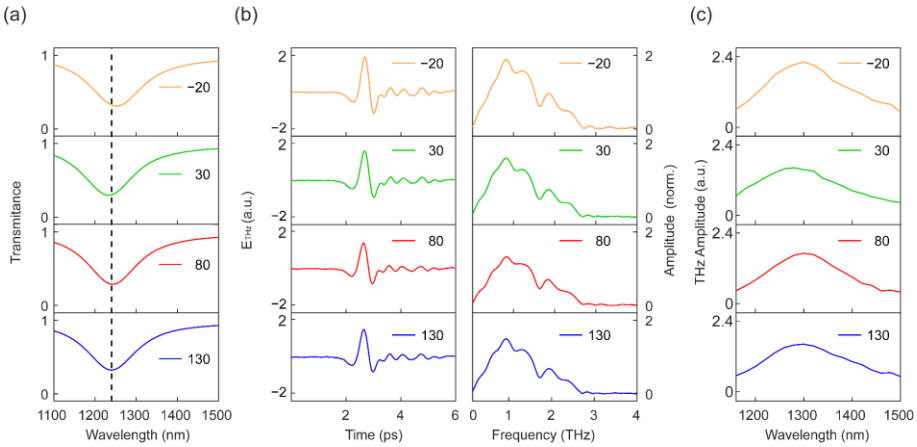

Figure S8. Linear and nonlinear responses of the achiral meta-molecules under *x*-polarized illumination. a) Measured linear transmission spectra. b) Measured THz pulses and their Fourier transform under 1240 nm FW pump. c) Measured THz peak-to-peak amplitudes with respect to the pump FW wavelength. The results in (b) and (c) are normalized to the corresponding maximum amplitudes in Figure 2e at $\Delta S = 130$ nm. The amplitudes of generated THz pulses are nearly the same and approximately two times larger than that of the maximum case under *y*-polarized pump.

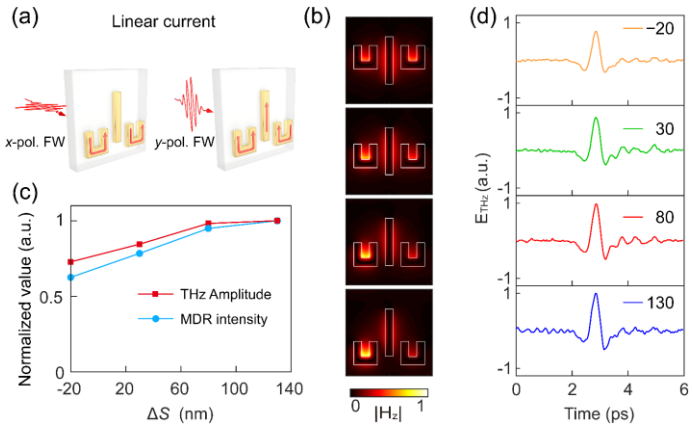

Figure S9. Linear and nonlinear responses of the achiral meta-molecules under circularly polarized illumination. a) Schematics of the linear surface current distributions on the achiral meta-molecules under the *x*- and *y*-polarized pump. b) Simulated H_z-field distributions at different ΔS from −20 nm (top) to 130 nm (bottom) under 1280 nm LCP pump. The different resonance strengths of the MDRs in the left and right SRRs can be attributed to the approximate constructive and destructive interference effects, respectively (see section 2.3 in the main text). c) Simulated overall MDR intensity and measured THz peak-to-peak amplitude at different ΔS, which clearly show very consistent varying trends in a normalized range. d) Measured time-domain THz pulses at different ΔS under 1280 nm LCP pump. Owing to the mirror symmetry of the achiral meta-molecules, the corresponding results under RCP pump are the same to those under LCP pump, except the resonance strengths of the left and right MDRs, where they will exchange their resonance behaviors.

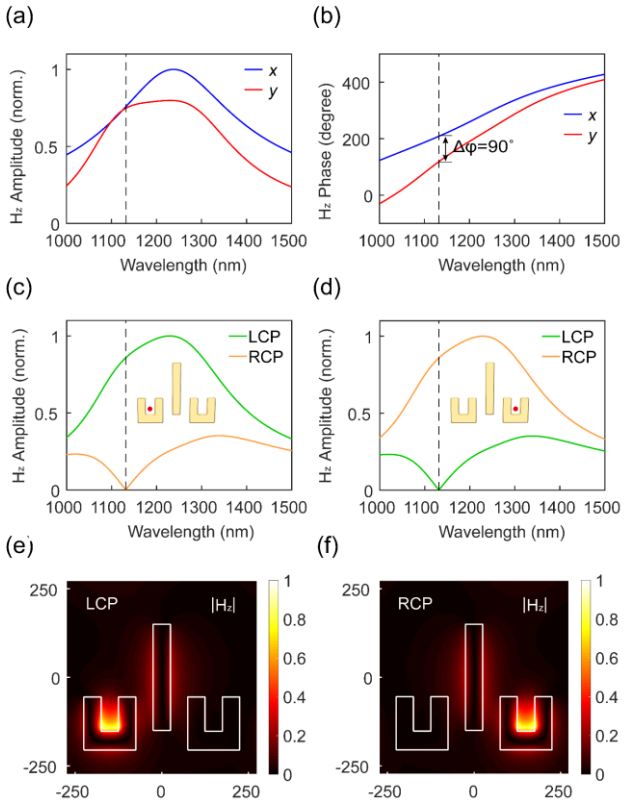

Figure S10. Near-field simulations of the achiral meta-molecule with Δ*S* = 130 nm. a,b) Normalized amplitude and phase spectra of the H_z fields at the center of the left SRR under *x*- and *y*-polarized illumination, respectively. The black dashed lines mark 1130 nm wavelength. c,d) Normalized amplitude spectra of the H_z fields at the center of the left and right SRRs under LCP and RCP illumination, respectively. e,f) H_z-field distributions under LCP and RCP illumination at 1130 nm wavelength, respectively.

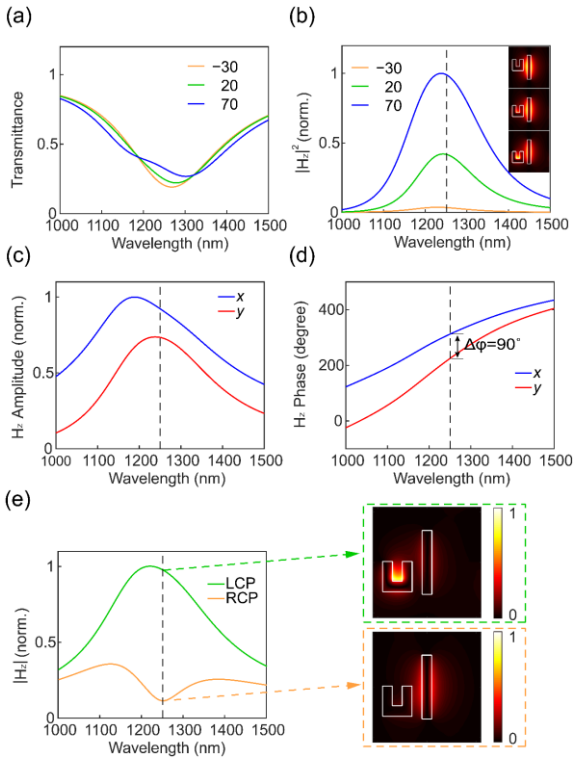

Figure S11. Simulated linear electromagnetic properties of chiral meta-molecules. a) Transmission spectra of chiral meta-molecules with ΔS changing from −30 nm to 70 nm under *y*-polarized illumination. b) Corresponding normalized near-field MDR intensity spectra $|H_z|^2$ recorded at the center of the SRR for different ΔS. The insets at the right corners are corresponding simulated H_z-field distributions at 1250 nm wavelength. c,d) Normalized amplitude and phase spectra of the H_z fields at the center of the SRR with ΔS = 70 nm under *x*- and *y*-polarized illumination, respectively. The inset dashed lines mark 1250 nm wavelength. e) Normalized amplitude spectra of H_z fields at the center of the SRR with ΔS = 70 nm under the LCP and RCP illumination. The color maps show the H_z-field distributions at 1250 nm wavelength. The small but non-zero H_z under RCP illumination is attributed to the slight amplitude difference in (c), which could be avoided by adjusting the coupling through changing ΔS.

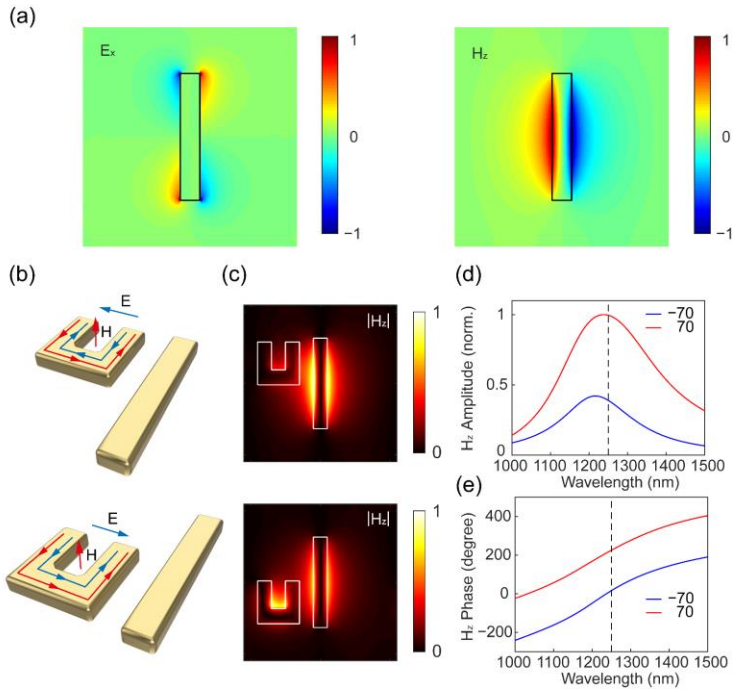

Figure S12. Evolution of the coupling effect as the SRR moves vertically along the bar. All panels show simulation results for *y*-polarized illumination. a) E_x- and H_z-field distributions of the solo bar resonator at 1250 nm wavelength, which dominate the electric and magnetic couplings towards the SRR, respectively. b) Schematic of the surface current distributions on the SRR due to the electric coupling (blue) and magnetic coupling (red) at $\Delta S = -70$ nm (top) and 70 nm (bottom). c) H_z-field distributions of the meta-molecules with $\Delta S = -70$ nm and 70 nm for pumping at 1250 nm wavelength. d,e) Normalized amplitude and phase of H_z at the center of the SRR as a function of pump wavelength for $\Delta S = -70$ nm and 70 nm.

References

[S1] W. Huang, J. Lin, M. Qiu, T. Liu, Q. He, S. Xiao, L. Zhou, *Nanophotonics* **2020**, 9, 3251.

[S2] M. Fang, K. Niu, Z. Huang, W. E. I. Sha, X. Wu, T. Koschny, C. M. Soukoulis, *Opt. Express* **2018**, 26, 14241.

[S3] F. Blanchard, L. Razzari, H. C. Bandulet, G. Sharma, R. Morandotti, J. C. Kieffer, T. Ozaki, M. Reid, H. F. Tiedje, H. K. Haugen, F. A. Hegmann, *Opt. Express* **2007**, 15, 13212.